Aalborg Universitet

AALBORG UNIVERSITY
DENMARK

Single-Frequency Phaseless Data Based Echo Suppression for Antenna Pattern Measurement in a Non-ideal Chamber

Wang, Heng; Wang, Weiming; Zhang, Fengchun; Wu, Yongle; Liu, Yuanan; Pedersen, Gert Frølund; Fan, Wei

Published in:
I E E E Transactions on Antennas and Propagation

Publication date:
2023

Link to publication from Aalborg University

Citation for published version (APA):
Wang, H., Wang, W., Zhang, F., Wu, Y., Liu, Y., Pedersen, G. F., & Fan, W. (2023). Single-Frequency Phaseless Data Based Echo Suppression for Antenna Pattern Measurement in a Non-ideal Chamber. *I E E E Transactions on Antennas and Propagation*.

General rights
Copyright and moral rights for the publications made accessible in the public portal are retained by the authors and/or other copyright owners and it is a condition of accessing publications that users recognise and abide by the legal requirements associated with these rights.

- Users may download and print one copy of any publication from the public portal for the purpose of private study or research.
- You may not further distribute the material or use it for any profit-making activity or commercial gain
- You may freely distribute the URL identifying the publication in the public portal -

Take down policy
If you believe that this document breaches copyright please contact us at vbn@aub.aau.dk providing details, and we will remove access to the work immediately and investigate your claim.

Single-Frequency Phaseless Data Based Echo Suppression for Antenna Pattern Measurement in a Non-ideal Chamber

Heng Wang, Weimin Wang, *Senior Member, IEEE,* Fengchun Zhang, Yongle Wu, *Senior Member, IEEE,* Yuanan Liu, *Member, IEEE*, Gert Frølund Pedersen, *Senior Member, IEEE*, and Wei Fan, *Senior Member, IEEE,*

***Abstract*—Antenna pattern measurement generally requires an anechoic chamber with a single ling-of-sight (LOS) propagation. However, it may not be satisfied due to cost and size limitations, leading to a non-anechoic environment (with echoes) and the distorted measured antenna pattern. To address this challenge, this paper proposed an echo suppression method using phaseless data at a single frequency. With the proposed method, one can discriminate the multipath characteristic convoluted with the actual antenna pattern by measuring the antenna gain pattern at multiple spatial locations. Different from the state-of-art methods requiring phase information, the proposed method is an amplitude-only technique, thus enabling cost-effective and true over-the-air (OTA) measurement for the wireless device. Furthermore, we derived a systematic guideline for the proposed method to improve measurement efficiency based on numerical simulations. The proposed method is experimentally validated by placing a metal plate in the chamber to emulate a non-anechoic environment, and a good agreement between the true antenna pattern and the reconstructed antenna gain pattern is found. Both numerical and experimental validations demonstrated the feasibility and robustness of the proposed technique.**

***Index Terms*—Antenna measurement, echo suppression, non-anechoic chamber, phaseless measurement, reference antenna.**

I. Introduction

ANTENNA measurement is essential to characterize and validate the radiation performance of the antenna under test (AUT) [1]. A large anechoic chamber, which can provide a clean line-of-sight (LOS) propagation path with a planar wavefront between the probe antenna and the AUT, is therefore required in the direct far-field (DFF) setup for accurate antenna pattern measurement. However, this often necessitates high-performance absorbers and a large anechoic chamber, which cannot be afforded by most research institutes and cannot be utilized for massive AUT testing. In addition, there are cases in which the disruptive echoes cannot be completely avoided due to, e.g., the proximity of the antenna placed to the chamber wall, the reflection from objects that cannot be covered by absorbers, or unsatisfactory performance of radio absorbers. All those factors would contribute to the multipath environment and the therefore distorted measured antenna pattern.

To cope with this problem, diverse echo suppression techniques have been proposed in the state-of-the-art works. Exploiting the fact that the LOS path travels with the shortest time compared to the other echoes, the contribution of the LOS path can then be extracted by gating the echo signals in the time domain, i.e., the time (soft) gating method [2] [3]. However, this strategy is also based on complex signal measurements and it typically requires a-prior knowledge of the scattering environment (to set the suitable frequency bandwidth) and large measurement bandwidth. Hardgating system is a promising gating type method [4][5] by using fast radio frequency (RF) switch to gate the echo signals. However, it also requires sufficient delay between direct LOS and scatter reflections. Moreover, it is expensive and only feasible for large CATR system [4] [5]. Based on the assumption that the signal can be decomposed into the sum of reasonable basic functions in the time or frequency domain, algorithms using smaller measurement bandwidth are proposed, e.g., the matrix pencil method (MPM) reported in [6] and the sparse time domain signal representation method in [7] [8] [9].

In recent years, various single-frequency echo suppression strategies have been developed to correct the antenna pattern distorted by the echoes. Examples of such techniques are based on the equivalent current [10] [11] [12], mathematical absorber reflection suppression (MARS) [13], test zone field compensation [14] [15], and inward and outward propagation waves [16]. However, these algorithms typically require many complex signal measurements.

It was derived in [17] [18] [19] that the antenna response measured in a non-anechoic chamber can be expressed as the convolution in the angular domain between the channel angular transfer function and the true antenna radiation pattern. If the chamber multipath spatial profile is known, the true antenna pattern can be extracted with deconvolution methodology. Thus, the key to this method is to obtain a chamber characteristic including the multipath information, i.e., complex amplitudes and angles of the multipath. References

(Corresponding author: *Wei Fan.*)

Heng Wang is with the Beijing Key Laboratory of Work Safety Intelligent Monitoring, Department of Electronic Engineering, Beijing University of Posts and Telecommunications, Beijing 100876, China, and also with the Antenna Propagation and Millimeter-wave Systems (APMS) Section, Department of Electronic Systems, Faculty of Engineering and Science, Aalborg University, 9220 Aalborg, Denmark. E-mail: hengw@es.aau.dk.

Weimin Wang, Yongle Wu, and Yuanan Liu are with the Beijing Key Laboratory of Work Safety Intelligent Monitoring, Department of Electronic Engineering, Beijing University of Posts and Telecommunications, 100876 Beijing, China. E-mail: wangwm@bupt.edu.cn, wuyongle138@gmail.com, bhtang@bupt.edu.cn, and yuliu@bupt.edu.cn.

Fengchun Zhang Gert Frølund Pedersen and Wei Fan are with the Antenna Propagation and Millimeter-wave Systems (APMS) Section, Department of Electronic Systems, Faculty of Engineering and Science, Aalborg University, 9220 Aalborg, Denmark. E-mail: fz@es.aau.dk; gfp@es.aau.dk; wfa@es.aau.dk.

[17] employed the MPM in the spatial domain to capture the environmental information and then remove the echo effects on the measured pattern in the post-processing step. Alternatively, the chamber characteristic can be extracted by a reference antenna as implemented in [18], and comprehensive experimental validations are presented in [19].

In [20] and [21], a hybrid post-processing technique, incorporating the time gating exploiting frequency diversity and the spatial filtering exploiting probe diversity, is proposed, and excellent performance was achieved even in highly reflective environments. However, it demands great setup flexibility and a large set of measurement locations to form a large virtual array. Moreover, complex-signal measurement is required for the proposed algorithms. The antenna pattern comparison (APC) method [22] is an effective technique to reconstruct the AUT pattern with phaseless measurement. However, the amplitude-only APC algorithm would fail to work properly when the amplitude level of the echoes relative to that of the LOS path is too high. Moreover, it was demonstrated in [22] that the conventional APC method requires a considerable number of measurement points, leading to long measurement time. The advanced APC method developed in [22] [23] can significantly relieves the limitations, yet it requires complex-signal measurement.

Although various antenna pattern reconstruction techniques have been developed, there are some limitations. The issues can be summarized as follows:

- The complex signal is generally required to reconstruct the true antenna pattern. However, the practical problem is that phase measurement is not feasible for over-the-air (OTA) measurement since the connection to the wireless device is not available.
- Most of the current single-frequency techniques demand a large number of measurement samples, which is unfavorable in practice since measurement efficiency is crucial.
- Although the pattern reconstruction methods with wideband measurement (e.g. time-gating methods) can save measurement time, the support frequency bandwidth of the AUT (especially the active device) is typically limited and insufficient for time-gating type techniques.

In this paper, a novel echo suppression using the single-frequency amplitude-only information is proposed for the two-dimensional (2-D) far-field (FF) antenna measurement in a non-anechoic chamber. In the proposed strategy, a reference antenna is first measured at different spatial locations to establish an environment factor which can then be used to restore the actual AUT pattern. The main contributions are as follows:

1) Different from the conventional measurement systems, the proposed methodology requiring power-only measurement neutralizes the need for complex-signal measurement. It simplifies the measurement requirement and diminishes the hardware cost. Power-only measurement is essential for enabling true OTA measurements of active radio devices since access to the antenna port (and thereby phase measurement) is not supported. It is envisioned that OTA testing is inevitable for future integrated radio systems. Power-only measurements are generally supported by both active (e.g., received signal power (RSP) reported by commercial radios) and passive antenna systems.
2) The proposed method is a single-frequency technique with no requirement on the support bandwidth of the device under test (DUT), which is attractive for commercial radios with a limited supported bandwidth.
3) Measurement efficiency is of key importance in antenna measurement. The proposed algorithm only requires a few measurement locations, which can be easily implemented with the help of a mechanical turntable and slider in a fully automatic manner.
4) Comprehensive studies on the algorithm are performed to derive exact measurement guidelines, including the virtual probe array aperture, the spacing between spatial locations, etc. Our analysis demonstrates that accurate antenna pattern reconstruction can be achieved with a few measurement locations.

The rest of this article is organized as follows. Section II outlines the relationship between the measured pattern and the multipath channel. In Section III, we illustrate the principle of the proposed technique. Section IV presents the numerical verification and the detailed discussions. In Section V, the measurement examples are given to validate the feasibility of our proposed technique. The conclusion follows in Section VI.

II. System Model and Problem Statement

The general DFF antenna measurement system is schematically shown in Fig. 1, where the AUT is rotated, and the signal response at different angles is recorded to obtain the antenna pattern. In the non-anechoic environment, however, multi-path caused by the electromagnetic scatterer will also interact with the antenna, creating interferences in the antenna response. In the following, the signal model and reference antenna pattern reconstruction method are discussed.

A. Signal Model

Considering the multipath effects, the measured AUT $A_{AUT}^{M}(\phi)$ pattern, neglecting the noise, can be expressed as:

$$A_{AUT}^{M}(\phi) = \sum_{l=1}^{L} a_l \exp(j\varphi_l) A_{AUT}(\phi - \phi_l), \tag{1}$$

where $A_{AUT}(\phi)$ is the true pattern of the AUT to be determined. L is the number of propagation paths including the LOS path. ϕ is the orientation of the AUT, with $\phi = 0^\circ$ denoting the AUT and probe antenna face-to-face aligned. a_l, ϕ_l, and φ_l are the amplitude, impinging angle, and phase of the lth propagation path, respectively, with $a_1 = 1$ and $\phi_1 = 0^\circ$ characterizing the LOS path. (1) can be considered as the spatial convolution of the true antenna pattern and the spatial channel response:

$$A_{AUT}^{M}(\phi) = A_{AUT}(\phi) * B(\phi), \tag{2}$$

where $*$ denotes the circular convolution operator, and $B(\phi)$ denotes the channel response vector that can be expressed as:

$$B(\phi) = \sum_{l=1}^{L} a_l \delta(\phi - \phi_l) \exp(j\varphi_l), \tag{3}$$

If the channel characteristics vector $B(\phi)$ is known a prior, the actual pattern $A(\phi)$ can be extracted from $A^M_{AUT}(\phi)$ via compensating out the channel vector $B(\phi)$ as detailed below.

B. Reference Spatial Deconvolution

We can perform the discrete Fourier transform (DFT) for (2) in the angular domain, and the convolution relationship can be transformed into the multiplication relationship:

$$\tilde{\boldsymbol{A}}^M_{AUT} = \tilde{\boldsymbol{A}}_{AUT} \cdot \tilde{\boldsymbol{B}}. \tag{4}$$

$\sim$ denotes the DFT operation. Thus if $\tilde{\boldsymbol{B}}$ is known, the component of the actual antenna pattern can be separated:

$$\tilde{\boldsymbol{A}}_{AUT} = \tilde{\boldsymbol{A}}^M_{AUT} / \tilde{\boldsymbol{B}}. \tag{5}$$

The division is implemented element-wise in the DFT vectors. The actual antenna pattern can be obtained by performing the inverse DFT (IDFT) for (5), and $\tilde{\boldsymbol{B}}$ can therefore be considered as the calibration factor. Obviously, the key to spatial deconvolution for the actual pattern is to obtain the calibration factor $\tilde{\boldsymbol{B}}$. Generally, there are two methods to obtain $\tilde{\boldsymbol{B}}$, i.e., chamber channel sounding method [17], and reference antenna method [19].

1) Chamber channel sounding method: By using the spatial MPM with the formed virtual array in the chamber (i.e. by moving a single antenna to several preset spatial locations and measuring the chamber channel response at each spatial location) [17], the environment multipath characteristics, i.e., the propagation angles, amplitudes, and phases can be obtained. $B(\phi)$ can be derived with (3) and then the calibration factor $\tilde{\boldsymbol{B}}$ is calculated with DFT operation. This method is effective and widely employed for channel parameter estimation in wireless communication [24]. However, the performance is affected by the virtual array aperture (i.e. the spatial resolution) and requires a high signal-to-noise ratio.

2) Reference antenna method: Another alternative to extracting the calibration factor is using a reference antenna with known pattern $A_{REF}(\phi)$. Specifically, we first perform the pattern measurement for the reference antenna in the non-anechoic environment, resulting in a measured pattern $A^M_{REF}(\phi)$ yielding:

$$A^M_{REF}(\phi) = A_{REF}(\phi) * B(\phi). \tag{6}$$

Applying DFT operation for (6), the calibration factor can be derived as:

$$\tilde{\boldsymbol{B}} = \tilde{\boldsymbol{A}}^M_{REF} / \tilde{\boldsymbol{A}}_{REF}. \tag{7}$$

With the channel environment unchanged, we can still measure the AUT pattern $A^M_{AUT}(\phi)$. By substituting (7) into (5), the actual pattern in the DFT domain can be reconstructed as:

$$\begin{aligned} \tilde{\boldsymbol{A}}_{AUT} &= \tilde{\boldsymbol{A}}^M_{AUT} / \tilde{\boldsymbol{B}} \\ &= \frac{\tilde{\boldsymbol{A}}^M_{AUT} \tilde{\boldsymbol{A}}_{REF}}{\tilde{\boldsymbol{A}}^M_{REF}}. \end{aligned} \tag{8}$$

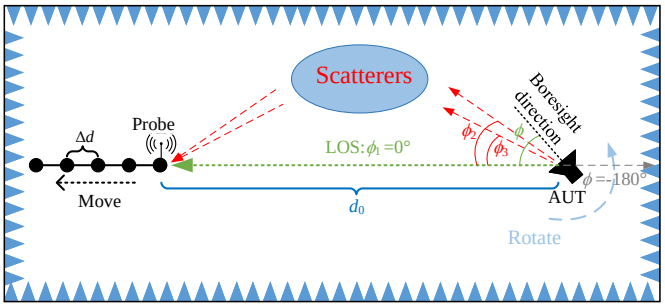

Fig. 1. The diagram of the FF antenna measurement in a non-anechoic chamber, where the AUT is rotated in a counterclockwise direction, starting from -180°, as dictated by the gray arrow.

Hence, $A_{AUT}(\phi)$ can be easily restored with the IDFT operation.

C. Problem Statement

The discussed reconstruction methodology based on spatial deconvolution is competent in recovering the actual antenna pattern measured in a non-anechoic environment with low-computational complexity, as demonstrated and experimentally validated in [18] [19]. The procedure of the spatial deconvolution technique is simple and does not require a complicated measurement campaign. Obviously, accurate channel characterization, in terms of propagation angles, amplitudes, and phases, is crucial for accurate AUT pattern reconstruction. Therefore the obtained channel response vector might be inaccurate in recovering the AUT pattern, leading to a distorted result. The exact error analyses are shown in Section IV. In addition, as mentioned before, phase measurement is not feasible for true OTA measurements, where cable connection to the AUT (which is required for phase and frequency synchronization) is not allowed. These motivate us to develop an echo suppression method based on amplitude-only measurements as the amplitudes and propagation angles of multipath are relatively stationary.

III. Proposed Amplitude-Only Echo Suppression

With only the amplitude data available at each ϕ, the reference spatial deconvolution method reported in [18] is no longer applicable. For this reason, a novel amplitude-only spatial deconvolution algorithm is proposed in this work as detailed below.

A. System Model

With the proposed method, the probe antenna placed in the FF of the AUT is moved along the LOS path direction to M positions spaced by Δd, as shown in Fig. 1. The amplitude of the propagation paths over multiple probe positions is generally distance dependent due to the free space path loss. However, since the far-field measurement setup is considered here and the probe virtual array aperture is much smaller compared to the FF measurement distance d_0, the path power divergence among the probe virtual array introduced by the

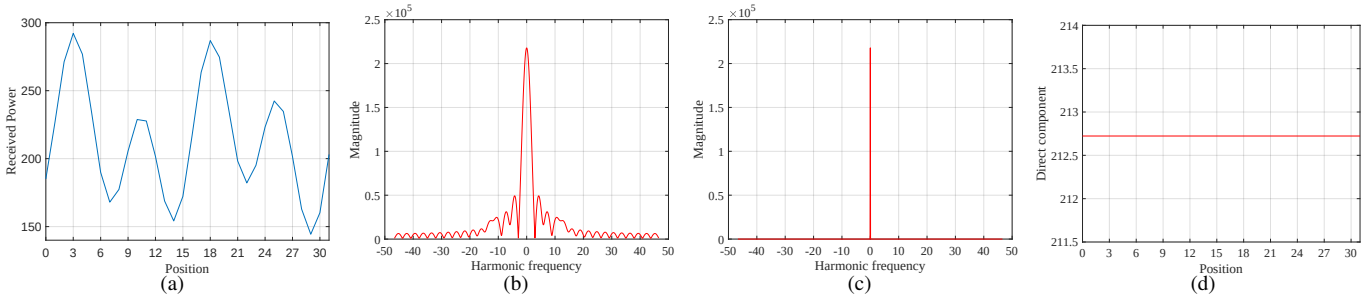

Fig. 2. An example of the extraction of the direct component. (a) Received power at different positions. (b) DFT for the received power. (c) After gating. (d) Direct component.

path loss is ignored. Neglecting the probe antenna pattern, with the measured antenna rotated to ϕ, the FF received signal is a vectorial summation of complex signals (composite field of direct path and reflected paths). It is determined by the multi-path channel and the antenna pattern of the AUT:

$$y(m,\phi) = \sum_{l=1}^{L} E_l(\phi)\cdot\exp(j2\pi k_l m\Delta d), \quad m = 0, ..., M-1. \tag{9}$$

where $E_l(\phi)$ is the complex amplitude of the lth propagation path at the original ($m = 0$) position with $E_1(\phi)$ denoting the contribution of the LOS propagation and can be expressed as:

$$E_l(\phi) = a_l \cdot |A(\phi - \phi_l)| \cdot \exp(j\Phi_l(\phi)). \tag{10}$$

$A(\phi)$ is the radiation pattern of the measured antenna. Φ_l is the received signal phase that is jointly determined by the lth wave propagation and antenna phase pattern response. k_l can be considered as the spatial frequency of the lth propagation wave along the direction of movement and can be expressed as:

$$k_l = \frac{cos(\phi_l)}{\lambda}. \tag{11}$$

The received power at the mth probe position for a given AUT rotation angle ϕ can be expressed as the squared magnitude of the complex received signal $y(m,\phi)$. Considering the non-anechoic environment with a LOS propagation and two reflection paths as an example, the received power $P(m,\phi)$ at the mth position for a given AUT rotation angle ϕ can be calculated as (12), where $(\cdot)^H$ is the conjugate operation. The terms I-III can be considered as the direct components, which are critical in our proposed method. The terms IV-VI can be considered as the harmonic components, which are characterized by the spatial frequency differences $(k_i - k_j)$ caused by the ith and jth propagation paths.

B. Proposed amplitude-only method

The critical part of the proposed method is to extract the direct components in (12). Taking a simulated measurement with $M = 32$ positions as an example, the specific procedure is detailed as follows:

1) Measure the received power at all M positions, and the power sequence is shown in Fig. 2(a).
2) Perform DFT for the obtained power sequence, and the harmonic frequency spectrum is shown in Fig. 2(b).
3) The direct components should appear at zero frequency. We should directly extract the harmonic spectrum value at zero frequency point. Specifically, by nulling the harmonic frequency components except that at zero frequency, as shown in Fig. 2 (c), the direct components in the DFT domain can therefore be obtained.
4) Perform IDFT for the obtained harmonic frequency spectrum after nulling operation in procedure 3. The desired direct components can be obtained, as exhibited in Fig. 2(d).

Perform the procedures 1-4 at each measured field angle ϕ, and the direct components can be obtained:

$$\Theta(\phi) = |E_1(\phi)|^2 + |E_2(\phi)|^2 + |E_3(\phi)|^2 + |\sigma(\phi)|^2. \tag{13}$$

where $|\sigma(\phi)|^2$ is the interference power component introduced by the spectrum leakages of the harmonic terms and is also the error source of the proposed method. It should be stressed that the scenario with $L = 3$ propagation paths is just taken as an example to illustrate equations (12) and (13) with the expanded form, and the extension to a more generic multipath propagation environment is straightforward and valid. According to (9) and (10), (13) can be rewritten as:

$$\begin{aligned}\Theta(\phi) &= \sum_{l=1}^{L} |E_l(\phi)|^2 + |\sigma(\phi)|^2 \\ &= \sum_{l=1}^{L} a_l^2 \cdot |A(\phi - \phi_l)|^2 + |\sigma(\phi)|^2 \\ &= \sum_{l=1}^{L} g_l \cdot T(\phi - \phi_l) + |\sigma(\phi)|^2.\end{aligned} \tag{14}$$

Thus (14) is a circular convolution of $\sum_{l=1}^{L} g_l\delta(\phi - \phi_l)$ and $T(\phi)$, as:

$$\Theta(\phi) = T(\phi) * G(\phi) + |\sigma(\phi)|^2, \tag{15}$$

with

$$T(\phi) = |A(\phi)|^2 \tag{16}$$

$$G(\phi) = \sum_{l=1}^{L} a_l^2\delta(\phi - \phi_l), \tag{17}$$

We can perform DFT for (15) in the rotation angle domain:

$$\tilde{\boldsymbol{\Theta}} = \tilde{\boldsymbol{T}} \cdot \tilde{\boldsymbol{G}} + \tilde{\boldsymbol{\sigma}}. \tag{18}$$

$\tilde{\boldsymbol{\sigma}}$ is the interference term $|\sigma(\phi)|^2$ in the DFT domain. As mentioned, we can employ a reference antenna to obtain

the chamber response characteristic $\tilde{\boldsymbol{G}}$, i.e., the environment factor. Specifically, $\Theta_{AUT}(\phi)$ and $\Theta_{REF}(\phi)$ are assumed to be the extracted direct components for each rotation angle from the AUT and reference antenna measurement, respectively, and $T_{REF}(\phi)$ is the known power pattern of the reference antenna. Thus the environment factor can be obtained via element-wise division:

$$\tilde{\boldsymbol{G}} = \tilde{\boldsymbol{\Theta}}_{REF} / \tilde{\boldsymbol{T}}_{REF}. \tag{19}$$

Thus the AUT power pattern in the DFT domain $\tilde{\boldsymbol{T}}_{AUT}$ can be calculated via element-wise division as:

$$\begin{aligned} \tilde{\boldsymbol{T}}_{AUT} &= \tilde{\boldsymbol{\Theta}}_{AUT} / \tilde{\boldsymbol{G}} \\ &= \frac{\tilde{\boldsymbol{\Theta}}_{AUT} \tilde{\boldsymbol{T}}_{REF}}{\tilde{\boldsymbol{\Theta}}_{REF}}. \end{aligned} \tag{20}$$

We can perform IDFT for $\tilde{\boldsymbol{T}}_{AUT}$ and then calculate the square root to recover the antenna gain pattern $|A_{AUT}(\phi)|$. For more accurate pattern reconstruction, a gating procedure should be performed to enhance the noise immunity before performing IDFT for $\tilde{\boldsymbol{T}}_{AUT}$, and the detailed analysis will be explained in section IV. Note that $|\sigma(\phi)|^2$ is undesirable to the circular convolution relationship between the channel angular power profile and the antenna power pattern, and its effects will be discussed in section IV in detail.

C. Summary

- We extract the direct component from (12) with the DFT transformation. Extracting the zero-frequency component in the DFT domain is equivalent to performing the average for the power sequence. The reason we perform the DFT procedure is for the error analysis. The investigation in the DFT domain provides insight into the undesired interference component, which helps us to study the algorithm error and derive the guideline of the virtual array design, as discussed in section IV.
- It should be stressed that there are two types of DFT implementation in the proposed algorithm. 1) For example, the AUT is assumed to be rotated from -180° to 179° with 1° spacing, and the power response is recorded for each rotation angle. Perform this measurement for M probe locations, and a $M \times 360$ power matrix can be obtained, where the mth row vector is the measured power pattern vector with the probe located at the mth location. The column vector is the power sequence measured at M probe locations with a certain rotation angle. In the proposed algorithm, we first perform the M-point DFT for the column vector sequentially to extract the direct component for each rotation angle, and a direct component vector composed of 360 elements is obtained. 2) In the spatial deconvolution procedure, i.e., (14)-(20), the 360-point DFT is implemented in the rotation angle domain to transform the spatial convolution as the dot multiplication of their DFT terms. It should be stressed that although the measurement campaign of the proposed method and that of the amplitude-only APC method [22] are similar, the target of multi-position measurement, the processed data, and principle of these two methods are different.
- The proposed algorithm adopts the known reference antenna to extract the environment factor rather than the channel sounding strategy for two reasons: First, most of the angle estimation algorithms require phase information which is unavailable for the discussed systems. Secondly, for the proposed recovery strategy, the environment factor obtained from the reference antenna outperforms that calculated with multipath properties, which will be demonstrated in the numerical analysis section. Different from the gain substitution method in antenna measurement community, the proposed method employ the reference antenna to extract the non-anechoic environment characteristics. In practice, reference antennas are known antennas, with well-characterized antenna radiation patterns. Reference antennas, e.g., standard gain horn antennas and corrugated horn antennas, are commercially available, and the information about their radiation patterns is accessible from the manufacturer data-sheet.

In the following, the factors that determine the algorithm performance, i.e., its feasibility, the impact of system uncertainty, its robustness, the relationship between the environmental characteristics and probe configuration, and how to select a reference antenna, are comprehensively investigated.

IV. Numerical Analysis

In this section, we simulated a non-anechoic environment to investigate the performance and robustness of the proposed

$$\begin{aligned} &P(m,\phi) = y(m,\phi) \cdot y^H(m,\phi) = \\ &|E_1(\phi)|^2 + |E_2(\phi)|^2 + |E_3(\phi)|^2 + E_1(\phi){E_2}^H(\phi) \cdot \exp(j2\pi(k_1-k_2)m\Delta d) + E_1(\phi){E_3}^H(\phi) \cdot \exp(j2\pi(k_1-k_3)m\Delta d) \\ &+ {E_1}^H(\phi)E_2(\phi) \cdot \exp(j2\pi(k_2-k_1)m\Delta d) + {E_1}^H(\phi)E_3(\phi) \cdot \exp(j2\pi(k_3-k_1)m\Delta d) \\ &+ E_2(\phi){E_3}^H \cdot \exp(j2\pi(k_2-k_3)m\Delta d) + {E_2}^H(\phi)E_3(\phi) \cdot \exp(j2\pi(k_3-k_2)m\Delta d) \\ &= \underbrace{|E_1(\phi)|}_{\text{I}} + \underbrace{|E_2(\phi)|}_{\text{II}} + \underbrace{|E_3(\phi)|^2}_{\text{III}} + \underbrace{2|E_1(\phi)||E_2(\phi)|cos(2\pi(k_1-k_2)m\Delta d + \Phi_1(\phi) - \Phi_2(\phi))}_{\text{IV}} \\ &+ \underbrace{2|E_1(\phi)||E_3(\phi)|cos(2\pi(k_1-k_3)m\Delta d + \Phi_1(\phi) - \Phi_3(\phi))}_{\text{V}} + \underbrace{2|E_2(\phi)||E_3(\phi)|cos(2\pi(k_2-k_3)m\Delta d + \Phi_2(\phi) - \Phi_3(\phi))}_{\text{VI}}. \end{aligned} \tag{12}$$

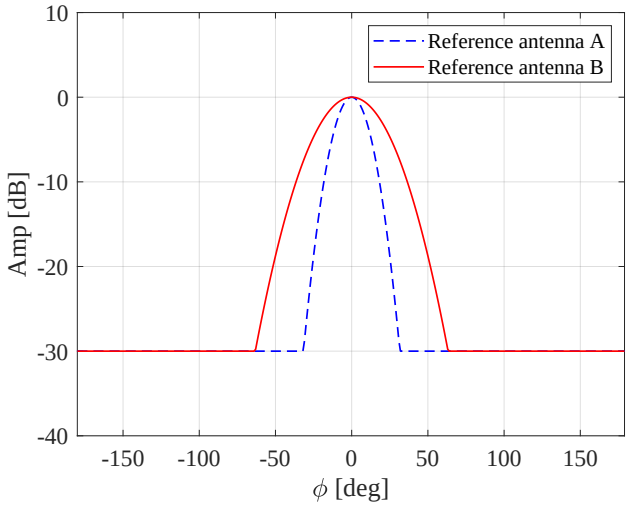

Fig. 3. The 3GPP synthetic patterns adopted for the reference antennas.

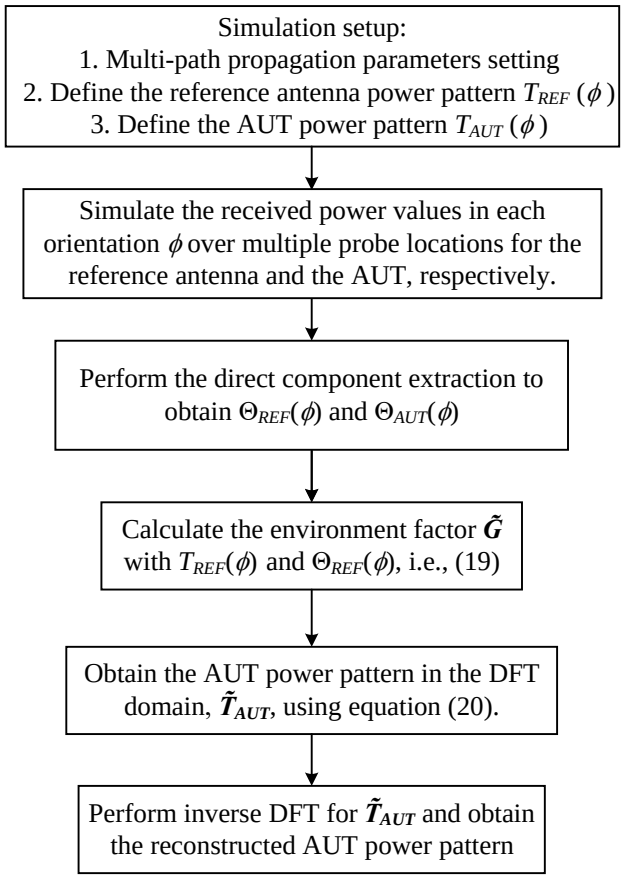

Fig. 4. The flowchart of the simulation framework.

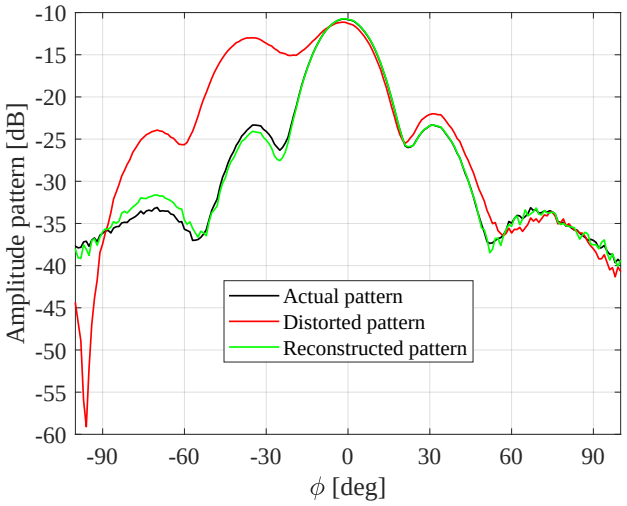

Fig. 5. Comparison between the actual pattern, pattern polluted with multi-path, and the pattern after applying the reflection suppression.

method. Specifically, 28 GHz is set to be the measurement frequency. An omnidirectional antenna is considered as the probe located in the ϕ_1 direction. In addition to the LOS propagation ($a_1 = 1$ (0 dB), $\phi_1 = 0°$), two reflection waves with $a_2 = 0.5$ (-6 dB), $\phi_2 = -40°$ and $a_3 = 0.3$ (-10.5 dB), $\phi_3 = -25°$ are presented to mimic a non-anechoic environment. A real measured horn antenna, with half-power beamwidth (HPBW) of 20°, is employed as the AUT. The red curve in Fig. 5 exhibits the distorted antenna pattern measured in a non-anechoic chamber, where neither the gain nor the pattern shape can be faithfully measured due to the echoes. It can be found that the peaks in the distorted region do not appear at the scatter angles ($-25°$ and $-40°$) but at the other angles ($-37°$ and $-70°$). The received signal is the coherent summation of the multipath signals. Due to limited antenna directivity, the received signals are not fully constructive summed or even in some cases are destructively summed at the scatterer angles ($-40°$ and $-25°$). With the AUT rotation, the phase of the received signals changes due to the antenna phase pattern, leading to peaks at angles of $-37°$ and $-70°$.

Two types of synthetic radiation patterns, specified by the 3GPP in [25, Table 7.3-1], with HPBWs of 20° (antenna A) and 40° (antenna B), are considered as the reference antenna for the proposed technique. The synthetic pattern is exhibited in Fig. 3, where the peak-to-minimum gain ratio is 30 dB. The direction of probe movement is along the ϕ_1 direction, and $M = 30$ positions are moved with $\Delta d = \lambda$ for the proposed strategy, where λ is the wavelength. The simulation settings are kept in the analysis unless otherwise stated. Fig. 4 presents the flowchart of the simulation framework.

Using the proposed echo suppression with reference antenna A, Fig. 5 shows that the radiation pattern is successfully recovered, in terms of the pattern shape, HPBW, and gain. Note that the results in this paper are without normalization; thus the main beam gain of the reconstructed pattern matches well with the target one.

A. Algorithm Analysis

1) Reliable region: In practical applications, noise introduced by the environment or measurement system is unavoidable. For this reason, we added the complex random noise to the simulated measurement with the SNR set to 40 dB, and performed the Monto Carlo simulation with 1000 realizations. Reference antenna A is adopted in this simulation. In most realizations, results similar to that shown in Fig. 5 can be obtained. However, in extreme cases, noticeable errors might

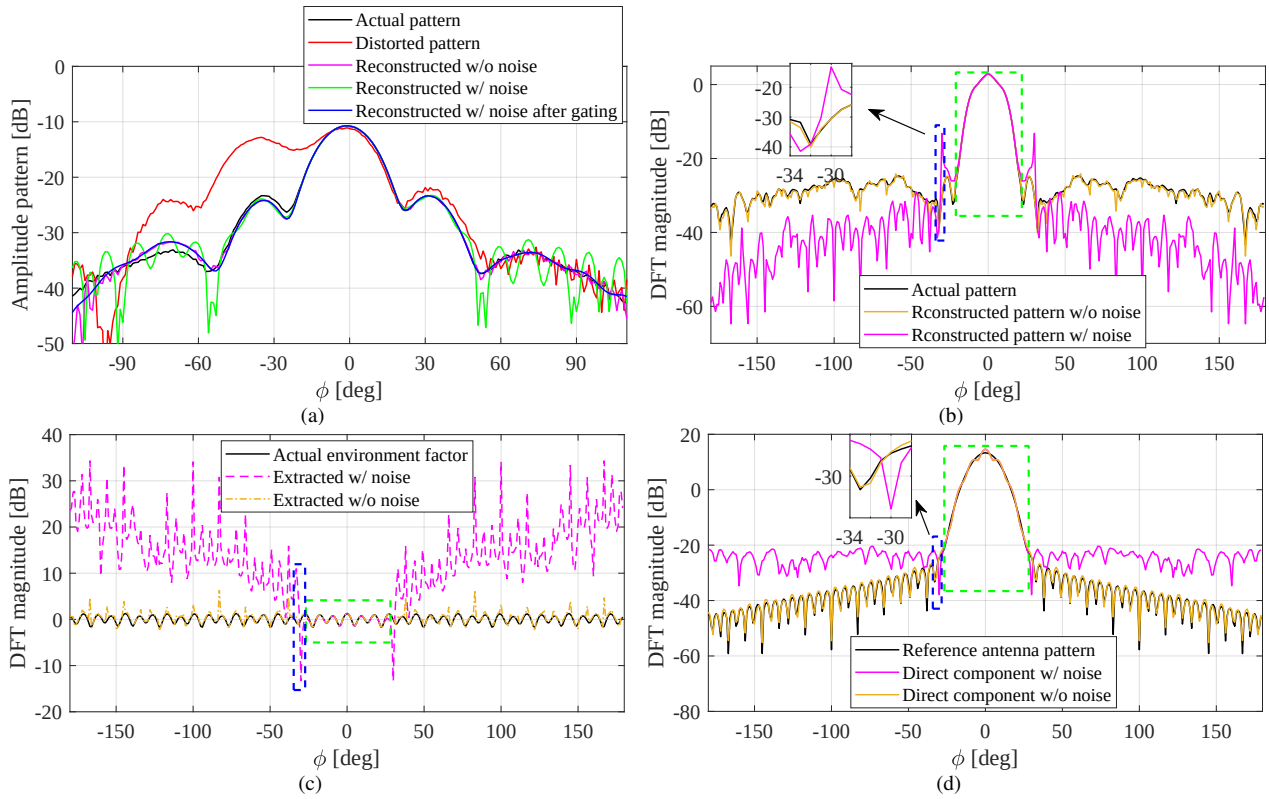

Fig. 6. Intermediate results of the proposed method with noise using reference antenna A. (a) Pattern comparison, where the pink and green curves are cases without and with noise, respectively. (b) Comparison of AUT patterns in the DFT domain. (c) Environment factor in DFT domain $\tilde{\boldsymbol{G}}$. (d) Component comparison of the reference antenna in the DFT domain. In figures (b)-(c), the yellow and pink curves are cases without and with noise, respectively.

emerge in weak signal directions (which are far from the main lobe direction in the antenna pattern). This is expected, since weak signals will be more sensitive to noise, compared to the main beam region, as shown by the green curve presented in Fig. 6(a). To thoroughly study the errors, Fig. 6(b)-(d) were provided to gain insights into the intermediate results in the DFT domain. It should be emphasized that since the DFT operation is performed for the pattern in the angular domain, the abscissa has no practical physical meaning and was still labeled as ϕ; this presentation is also adopted in [17]. According to the Fourier transform theorem, the components far from 0° are high-frequency components. Thus the more directive the pattern, the more high-frequency components exist.

Fig. 6(b) presents the comparison between the actual and reconstructed AUT power patterns, with and without noise, in the DFT domain, and all the curves match well within the green rectangle region, which is named the reliable region in the following. However, significant deviations can be observed outside the reliable region in the scenario with noise, especially in the blue rectangle region where the components (referred to as the spurious components in the following) present considerable power. Actually, the spurious components are the main cause of the degenerated performance since the other high-frequency components deviated from the target contribute little to the pattern due to the negligible power. The spurious components are introduced by the incorrect environment factor, as shown in Fig. 6(c). Compared to the actual environment factor and that extracted without noise, the curve of the environment factor extracted with noise presents significant deviations outside the green rectangle region. The components in the blue rectangle, combined with the division calculation in (20), cause the spurious components in Fig. 6(b). The incorrect environment factor estimation can be explained by Fig. 6(d). In some extreme cases, the noise will severely distort the extracted direct components in the DFT domain outside the reliable region (green rectangle region) of the reference antenna. As shown in the blue rectangle region in Fig. 6(d), the direct components can be reduced by about 17 dB due to the noise compared to the measurement without noises, leading to incorrect environment factor extraction.

This problem, nevertheless, can be easily tackled. Since most power of the reconstructed pattern in the DFT domain is concentrated within the reliable region (about 99.3% power), where the noises can be considered to be insignificant, the radiation pattern can be recovered by the spectrum components within the reliable region. Applying a rectangular window for the obtained pattern in the DFT domain, i.e., gating the components outside the reliable region, the recovered pattern is shown as the blue curve in Fig. 6(a). The window width can be easily determined from the DFT pattern. Specifically, when the power of the DFT pattern jumps to a low level, the window is truncated. Alternatively, if the contained power ratio reaches a threshold, the window is truncated. In the following discussion, the gating procedure is always applied.

2) Reference antenna selection: Fig. 7 presents the comparison of the proposed strategy using reference antenna A and B, where antenna B has a larger HPBW compared to the

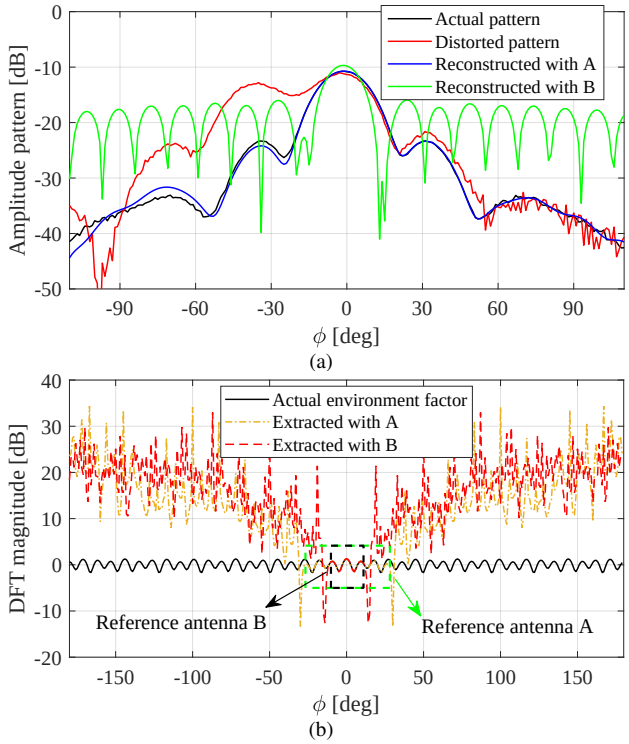

Fig. 7. Comparisons of the proposed method with noise using reference antenna A and B. (a) Reconstructed pattern comparison. (b) Environment factor in DFT domain $\tilde{\boldsymbol{G}}$ extracted with reference antenna A and B. The green and black rectangles are the reliable regions offered by different reference antennas for $\tilde{\boldsymbol{G}}$.

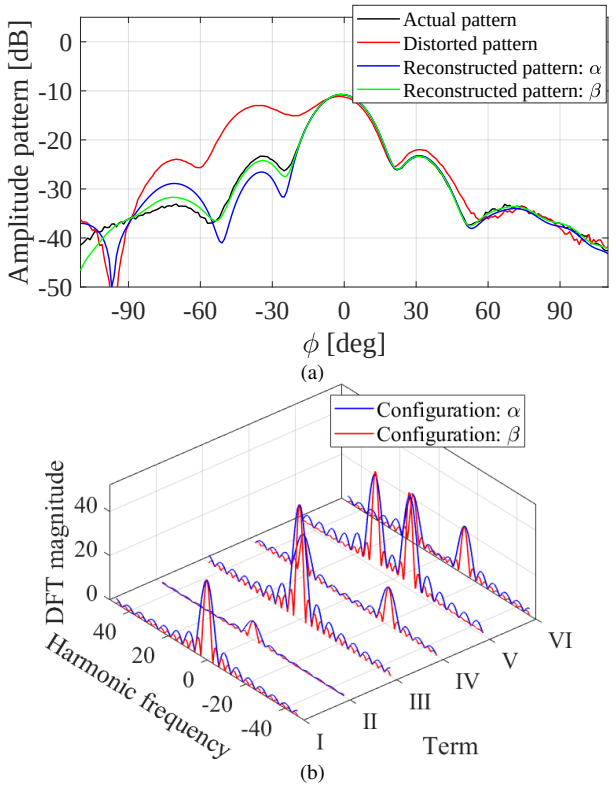

Fig. 8. Reconstructed pattern and the harmonic frequency spectrum analysis with different lengths of the virtual probe array. (a) Reconstructed patten. (b) Harmonic frequency spectrum.

AUT. It is shown in Fig. 7(a) that the proposed algorithm with reference antenna B would not work, and the gating operation will not help improve the results. It is known that a less directional antenna will have a narrower main lobe in the DFT domain. Thus, due to the narrow reliable region, the accurate region of the environment factor extracted from the reference antenna B will be narrower compared to the reference antenna A. Fig. 7(b) shows the environment factors extracted with reference antenna A and B. As expected, reference antenna B offers a narrower reliable region (black rectangle), leading to spurious components in the AUT DFT pattern appearing in the position close to 0°, which cannot be filtered by gating. For the proposed algorithm, it can be deduced that the reliable region of the reference antenna should be broader than that of the AUT. In other words, the reference antenna should be more (at least equally) directional than the AUT.

B. Zero-frequency pollution

Ideally, the harmonic components in (12) should be delta-shape impulse responses in the DFT domain. It is, however, not the case since the length of the power measurement sequence from the virtual probe array is finite in practice. As a result, the power leakage in the frequency spectrum is unavoidable and will create interfering power on the zero frequency in the DFT domain, introducing undesired components $\tilde{\boldsymbol{\sigma}}$ to $\tilde{\boldsymbol{\Theta}}$. The interfering power caused by the spectrum leakage is referred to as zero-frequency pollution in this paper. In this part, we discuss how zero-frequency pollution would affect our algorithm and how to mitigate the adverse effects. Reference antenna A is employed here.

1) Sampling length: It is known that the spectrum leakage is determined by the length of the processed sequence. Generally, the longer the length, the less leakage will be [26]. However, longer length also means more measurement locations and therefore longer measurement time. Adopting the same moving step $\Delta d = \lambda$, Fig. 8(a) shows the reconstructed antenna pattern using the proposed method with different apertures of the virtual array. Two configurations are considered here, i.e., case α: 15 probe positions, and case β: 30 probe positions. It can be found that noticeable accuracy degeneration can be observed in configuration α compared to that with $M = 30$ probe positions. This phenomenon can be explained by Fig. 8(b), which shows the individual harmonic frequency spectrum of all the components in (12) at a certain field angle, and the term labels in the figures are consistent with that marked in (12). As expected, the components in the DFT domain act in the form of the Sinc function [26]. When the larger sampling length is adopted, all the components in the harmonic frequency spectrum become closer to the Dirac impulse, and less zero-frequency pollution will be introduced. Thus forming a large virtual probe array for the proposed algorithm is an efficient strategy to reduce zero-frequency pollution and improve the recovery accuracy.

2) Window function: The zero-frequency pollution is not only determined by the length of the virtual probe array but also by the multipath angles. The harmonic frequencies in (12) are the spatial frequency differences, $(k_i - k_j)$, between the

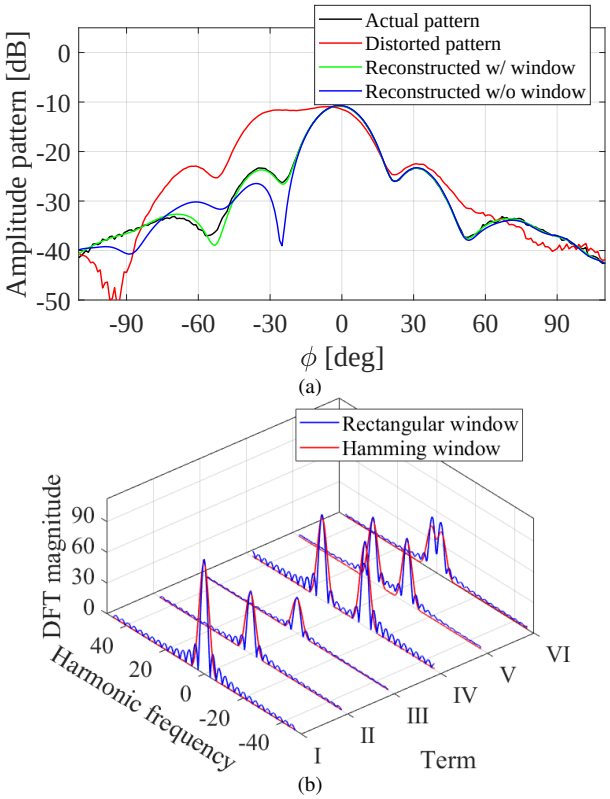

Fig. 9. Reconstructed pattern and the harmonic frequency spectrum analysis with and without window function. (a) Reconstructed pattern, where the blue and green curves are cases without and with Hamming window, respectively. (b) Harmonic frequency spectrum.

LOS path and echoes (terms IV and V) and between echo and echo (term VI). Thus if the angles of two propagation paths are close, the corresponding harmonic frequency approaches 0, leading to more zero-frequency pollution. With a given virtual probe array, the proper window function can be employed for the measured power sequence at each field angle to mitigate the spectrum leakage [26] and the associated zero-frequency pollution. ϕ_2 is changed to $-28°$ in this part to simulate a scenario with close propagation angles. Fig. 9 shows the reconstructed pattern and the individual harmonic frequency spectrum when the window function is applied and not applied. Since ϕ_2 is closer to ϕ_1 compared to the previous simulation, a more significant spectrum leakage of term IV can be observed in Fig. 9(b). Thus the reconstructed pattern is distorted in the low-power region, which is relatively fragile. Employing the Hamming window [26] for the power sequence for each rotation angle ϕ (characterized by equation (12)), red curves in Fig. 9(b) demonstrate that the side lobe of the Sinc function is suppressed, and thus the spectrum leakages caused by terms IV and V are effectively reduced. Then the extracted direct components are cleaner, and the recovered pattern can be significantly improved, as shown in Fig. 9(a). It is well known that Hamming window is superior to the rectangular window in reducing spectrum leakage since it can help make the power sequence more periodic.

Applying the window function not only can help suppress the side lobes but, on the other hand, it also enlarges the width of the main lobe in the DFT domain. Term VI in Fig. 9(b) exhibits that the main lobes more severely overlap due to the window function, leading to more power leakage at the zero frequency. To tackle this problem, we generally need a larger measurement probe array aperture. However, terms IV and V are the dominant interferences, and the effects from term VI, even with high power, can be removed in the proposed algorithm. To explain the reason, we first define the harmonic components caused by the paths far apart as harmonic A, such as term IV and V. The harmonic components caused by the close paths are defined as harmonic B, such as term VI. Since the propagation angles of harmonic B are adjacent, the following approximation holds:

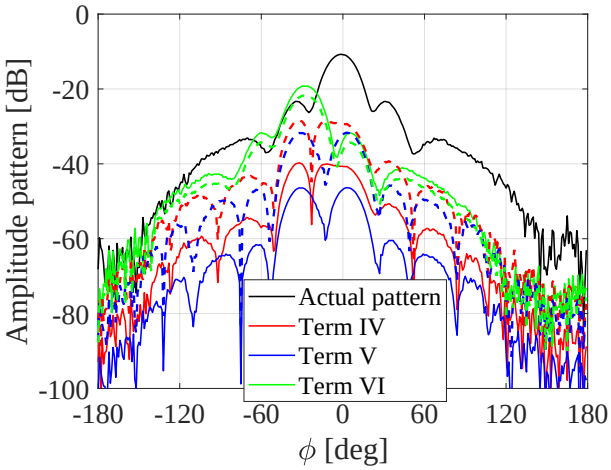

Fig. 10. Power leakages caused by the harmonic components. The solid lines are in the cases with Hamming window, and the dashed lines are in the cases without the window.

$$\begin{aligned} |E_2(\phi)||E_3(\phi)| &= a_2a_3|A(\phi-\phi_2)||A(\phi-\phi_3)| \\ &\approx a'|A(\phi-\phi')|^2, \end{aligned} \tag{21}$$

where $\phi' \in [\phi_2, \phi_3]$ and $a' = a_2a_3$. The cosine term in (12) can be approximated as:

$$\begin{aligned} &cos(2\pi(k_2-k_3)m\Delta d+\Phi_2(\phi)-\Phi_3(\phi)) \\ &= cos(2\pi(k_2-k_3)m\Delta d+\varphi_2-\varphi_3+\overline{\Phi}(\phi-\phi_2)-\overline{\Phi}(\phi-\phi_3)) \\ &\approx cos(\varphi_2-\varphi_3) = c. \end{aligned} \tag{22}$$

where c is a constant. $\overline{\Phi}(\phi)$ is the phase response of the measured antenna. Since the propagation angles of harmonic B are close, the spatial frequencies, i.e., k_2 and k_3, of which are almost equal. Similarly, the same goes for the phase responses contributed by the antenna for adjacent paths. Thus:

$$2\pi(k_2-k_3)m\Delta d+\overline{\Phi}(\phi-\phi_2)-\overline{\Phi}(\phi-\phi_3) \approx 0. \tag{23}$$

Then (22) holds. Based on (21) and (22) the term VI in (12) can be rewritten as:

$$\begin{aligned} &2|E_2(\phi)||E_3(\phi)|cos(2\pi(k_2-k_3)m\Delta d+\Phi_2(\phi)-\Phi_3(\phi)) \\ &\approx c'|A(\phi-\phi')|^2 = |E_p(\phi)|^2. \end{aligned} \tag{24}$$

leading to the antenna pattern lifted up and down, where $c' = ca_2a_3$. (14) can be then rewritten as:

$$\begin{aligned}&\Theta(\phi)\\&=|E_1(\phi)|^2+|E_2(\phi)|^2+|E_3(\phi)|^2+|E_p(\phi)|^2+|\sigma(\phi)|^2\\&=\sum_{l=1}^{L} a_l^2\cdot|A(\phi-\phi_l)|^2+|E_p(\phi)|^2+|\sigma(\phi)|^2\\&=\sum_{l=1}^{L} a_l^2\cdot|A(\phi-\phi_l)|^2+c'|A(\phi-\phi')|^2+|\sigma(\phi)|^2\\&=\sum_{l=1}^{L+1} g_l\cdot T(\phi-\phi_l)+|\sigma(\phi)|^2.\end{aligned} \tag{25}$$

where $g_{L+1} = c'$ and $\phi_{L+1} = \phi'$. Thus the component of harmonic B can be accounted for as a "pseudo-path", and its contribution $|E_p(\phi)|^2$ will not damage the spatial convolution relationship. To examine whether the approximation of (24) is exactly valid, Fig. 10 presents the power leakages of terms IV-VI at different field angles. As expected, the evaluation of VI approximated the shifted and scaled actual pattern, while terms IV and V, which are disruptive to the spatial convolution relationship, are significantly suppressed with the window function. Thus the spatial convolution shown by (15)-(17) still holds, and an accurate pattern is recovered in Fig. 9(a). The characteristics of the pseudo-path can be extracted with the reference antenna as well, while the channel estimation-based chamber characterization does not. Thus the reference antenna method is more suitable for the proposed algorithms.

Note that not all the harmonic components caused by the paths with approximate spatial frequencies can be considered as harmonic B. For example, in the scenario with echoes symmetric with respect to the virtual probe array, e.g. from $-25°$ and $25°$, severe zero-frequency pollution will destroy the spatial convolution relationship since (21) does not hold. This will lead to distorted pattern reconstruction. In such scenarios, one can adjust the direction of probe movement to make the harmonic components as far as possible from the zero-frequency to reduce the interference, as the spatial frequencies of propagation paths are determined by not only the multipath properties but also the direction of probe movement. For instance, when the probe moves along the direction perpendicular to the LOS path, the spatial frequencies of echoes with $-25°$ and $25°$ will be k_i and $-k_i$, and the resulting harmonic frequency would be $\pm 2k_i$ and far from the zero frequency point in the DFT domain. Therefore, one can employ a 2-D virtual probe array to improve the spatial resolution (performance) of the proposed method. Otherwise, one can exploit the wideband information to distinguish the echoes in the delay domain, which will be our future research.

3) The required length of probe movement: It is worth noting that the approximations of (21)-(25) are based on the assumption that the associated propagation paths are close. Otherwise, the length of the virtual probe array should be large enough to avoid the main lobe overlap. If the length of probe movement is D, the spatial bandwidth is $1/D$. Fig. 11 shows one harmonic spectrum with Hamming window in the DFT domain, where the lobe width with the Hamming window should be $B = 2/D$. $\tilde{k}$ is assumed to be the minimum harmonic frequency A. To avoid the overlap, obviously, D should satisfy:

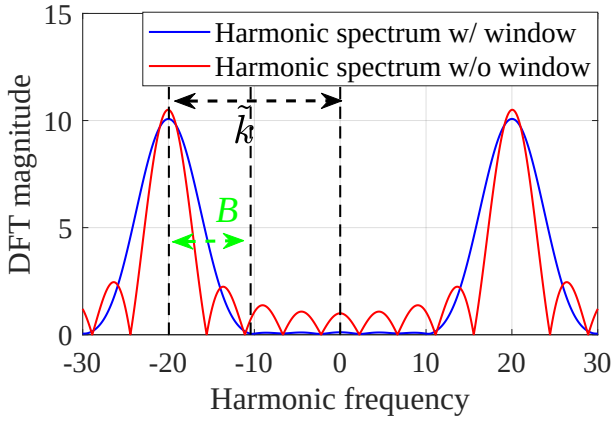

Fig. 11. Analysis of required length of the virtual array.

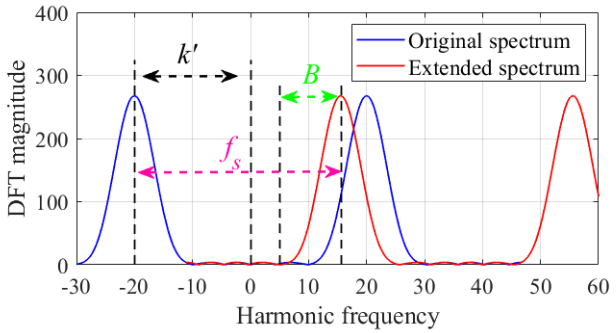

Fig. 12. Analysis of spectrum aliasing of the proposed method.

$$B = 2/D < \tilde{k} \tag{26}$$

$$D > \frac{2}{\tilde{k}} \tag{27}$$

(27) aims to offer a practical guideline for the required distance of the probe movement. In practice, $\tilde{k}$ is typically unknown. It can be found that the selection of D depends on the differences in the impinging angle of propagation paths. A large separation would need a small D. In practice, if we can roughly estimate the dominant echoes in the environment, we can set D accordingly.

4) The number of probe positions (probe spacing): In practice, however, moving the probe to too many positions typically requires extensive measurement time and is unfavorable. In this part, the relationship between the number of probe positions and the algorithm accuracy is derived. It is well known from Fourier transform that the sequence length determines the lobe width and decaying rate of the Sinc function in the DFT domain, while for a fixed sequence length the number of sampling points, i.e., sampling rate, determines the spectrum aliasing in the DFT domain. With given probe movement length D, the sampling rate is $f_s = (M-1)/D$. k' is assumed to be the maximum harmonic frequency in (12). Different from the other signal processing algorithm which should satisfy Nyquist Sampling Theorem to avoid spectrum

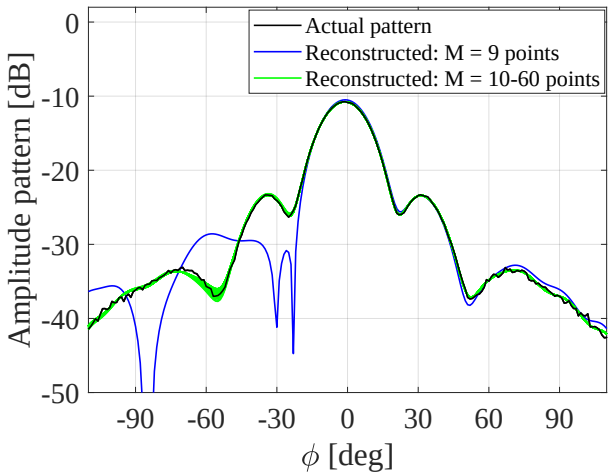

Fig. 13. The recovered patterns using the probe moved with 9-60 points.

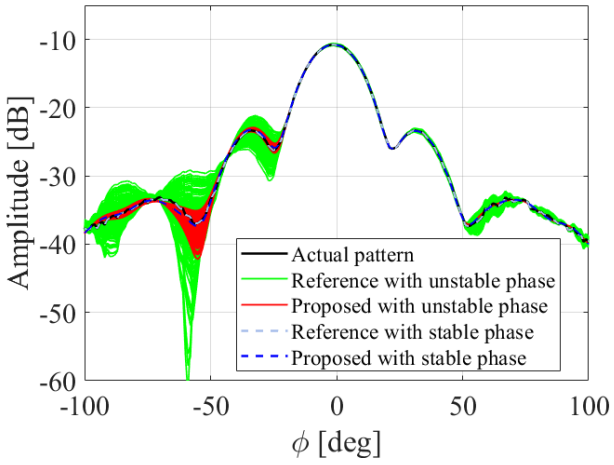

Fig. 14. The recovered patterns for the 200 realizations with the conventional spatial deconvolution algorithm and the proposed algorithm, using the data with and without phase noises.

aliasing in the DFT domain, the proposed method is concerned with zero frequency fidelity, and the aliasing at other frequency points is insignificant. Fig. 12 shows an example of the harmonic spectrum and the periodically extended spectrum caused by the finite Fourier transform, where the Hamming window is employed. It can be found that though spectrum aliasing exists, the zero frequency point is unaffected as well. Thus we can deduce a criterion that the sampling rate should satisfy:

$$f_s > k' + B \tag{28}$$

In other words:

$$\begin{aligned} M = f_s D + 1 &> (k' + B)D + 1 \\ &= k'D + BD + 1 \\ &= k'D + 3 \end{aligned} \tag{29}$$

To validate this inference, we configure that $D = 60\lambda$, $\phi_2 = -28°$, and $\phi_3 = -25°$, and the other parameters are unchanged. In this scenario, $Dk' + 3 = 9.9$, while 19 probe positions are required according to the Nyquist Sampling Theorem. Fig. 13 shows the recovered pattern for the different realizations with 9 to 60 uniformly sampled probe positions with the given D. It can be found the result with 10 probe positions offers satisfying accuracy as expected. Using criterion (29), the measurement time can be significantly saved. Even if the maximum harmonic frequency is unknown in practice, one can assume a safe threshold according to the chamber geometry and the multipath profile recorded with the reference antenna.

5) Robustness: During a long measurement period, the chamber environment (especially the phase measurement) may not remain stationary. Thus the phases of propagation paths are unstable, which, therefore, are detrimental to the reference (Section II. B) spatial deconvolution requiring accurate phase information [18]. Fig. 14 shows the reconstruction results with the reference and proposed method for 200 realizations, where the unstable phase is the case where rather small random phase deviations ranging from $-3.6°$ to $3.6°$ are added. In this simulation, $D = 60\lambda$, $\phi_1 = -28°$, $\phi_2 = -25°$, and 10 probe positions are moved as before. It can be found that in the ideal scenario, the reference method presents excellent accuracy, while the performance significantly degenerates when the measurement environment is changed, even for a rather small phase variation. However, the proposed method is relatively insusceptible to the unstable phases, especially in the main beam and first side lobe regions. Although the proposed method does not need phase information, the phase deviations are associated with the impacts of zero-frequency pollution and pseudo path, leading to variations of the recovered pattern.

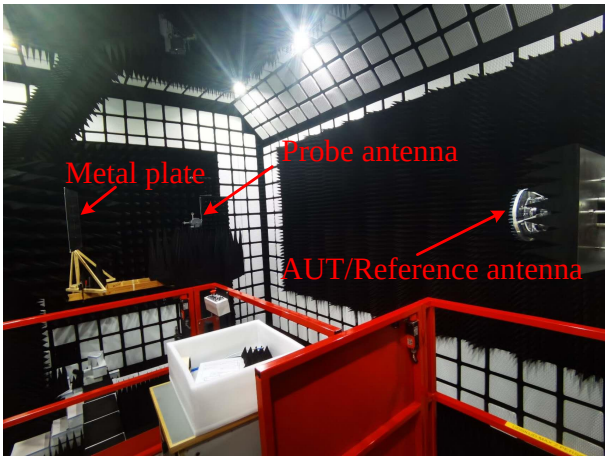

Fig. 15. The experimental setup in a non-anechoic scenario.

V. Experimental Validation

A. Measurement Campaign

The measurements are carried out in a large anechoic chamber at Aalborg University. The test scenario is shown in Fig. 15, where a metal plate with the size of $1\times1m^2$ is laid out to construct a non-anechoic environment. The plate location is configurated to create strong reflection paths towards the probe. Probe and AUT adopted the LGF-11-1800-WB-DL antenna with HPBW of $40°$, as shown in Fig. 16(a), as receiver and transmitter, respectively. A standard gain horn antenna Flann 22240-20 with HPBW of $20°$, as shown in Fig. 16(b), is employed as the reference antenna to extract the chamber

characteristics. 28 GHz is the measurement frequency, and λ_b is the wavelength. The virtual probe array implementation in our validation measurement can be summarized as the following steps:

(1) Place the reference antenna with a known gain pattern on the turntable, as shown in Fig. 15.
(2) Move the probe antenna to the first spatial location, as shown in Fig. 15, where the distance from the probe to the reference antenna (or AUT) is $9.22m$ in our measurement setup.
(3) The reference antenna is rotated in the azimuth plane and measured for the first spatial location.
(4) Repeat the antenna pattern measurement for probe antenna in other spatial locations with the help of a slider sequentially, and obtain the received power response of reference antenna $P_{REF}(m, \phi)$ for all spatial locations, i.e., equation (12). The slider (movement) direction is along the LOS path propagation. In our measurement, the probe is moved to $M = 38$ points with $\Delta d = 0.5\lambda_b$ covering the $19.82cm$ measurement range.
(5) Replace the reference antenna with AUT, as shown in Fig. 15. Repeat the procedures (1)-(4) for the AUT to obtain the received power response of AUT $P_{AUT}(m, \phi)$ for all spatial locations, i.e., equation (12).

In the above measurement campaign, only one minute is required to measure the AUT or reference antenna in 2-D azimuth plane at one probe position. The power divergence of propagation path among the probe array caused by the free-space path loss is no more than 0.18 dB and can be ignored. To examine the environment characteristics, the AUT is rotated and measures the frequency response at 28–30 GHz using a vector network analyzer (VNA), where 101 frequency points are recorded at each field angle. It should be stressed that this wideband complex signal measurement aims to show the power angle delay profile (PADP) of the employed non-anechoic environment for readers, and only single-frequency amplitude-only data at 28 GHz is utilized for the algorithm processing. Fig. 17 shows the measured PADP. Apart from the LOS path and reflection, there also exist some weaker propagation paths, as indicated by the yellow arrow, which might be caused by system non-ideality, the scattering path caused by the setup components, and the diffraction paths introduced by the edges of the plate. Particularly, it can be found a path appears before LOS. It is a signal path that should be introduced by the loose connector behind the probe antenna or insufficient isolation between the transmitter and receiver. Furthermore, it can be deduced that the diffraction paths might be from not only the 2-D plane but also the 3-D direction, due to the top and bottom edges of the plate. Note that the results here are without normalization to demonstrate the agreement between gain reconstruction and the actual antenna gain.

B. Validation Results

For the algorithm validation, the reference antenna and AUT are first measured in the anechoic chamber and then measured at 28 GHz in the constructed non-anechoic environment for the preset 38 probe locations. The antenna pattern measured in a

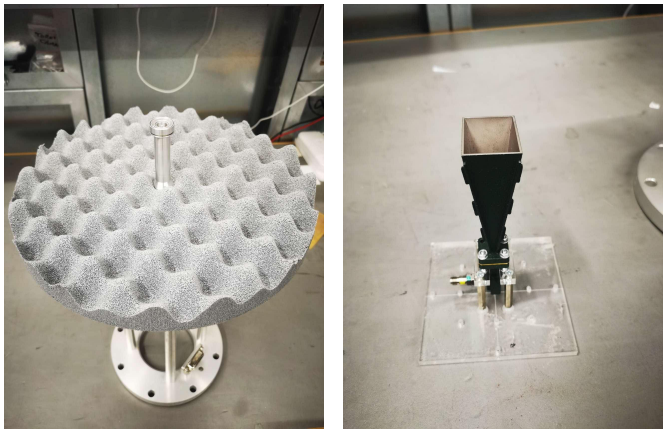

(a) (b)

Fig. 16. Photographs of (a) the probe (AUT) antenna and (b) the reference antenna.

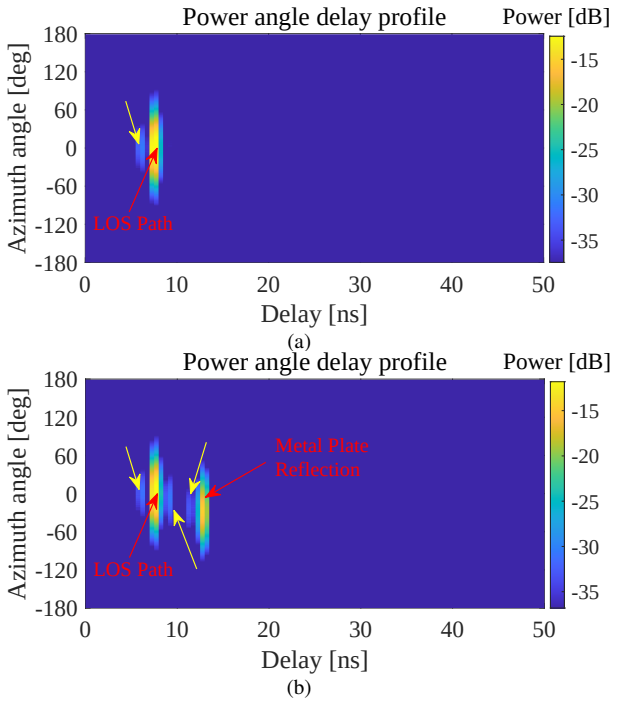

Fig. 17. PADPs of the (a) anechoic and (b) non-anechoic chamber environments.

non-anechoic chamber is shown in Fig. 18, where the red curve indicates that due to the multipath interference, -20 dB gain deviations are caused in the region around $-30°$. Furthermore, the gain, HPBW, and location of the main beam cannot be accurately measured. Adopting the proposed processing algorithm, Fig. 18 shows that a significant improvement of the antenna pattern can be achieved, and the amplitude gain of the main beam is well recovered. Slight deviations at the angles about $-100°$ can be caused by measurement uncertainty and zero-frequency pollutions. In addition, marginal discrepancy appears in the regions of $\phi = -130° \sim -180°$ and $130° \sim 180°$, which is attributed to the low signal-to-noise ratios in these regions in the measurement.

To examine the inference about the required numbers of probe positions, different sets of probes are employed for algorithm validation. The maximum harmonic frequency is

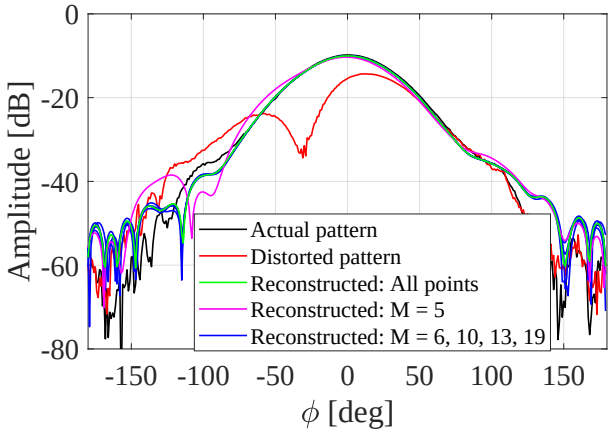

Fig. 18. The reconstructed pattern using different sets of probe positions.

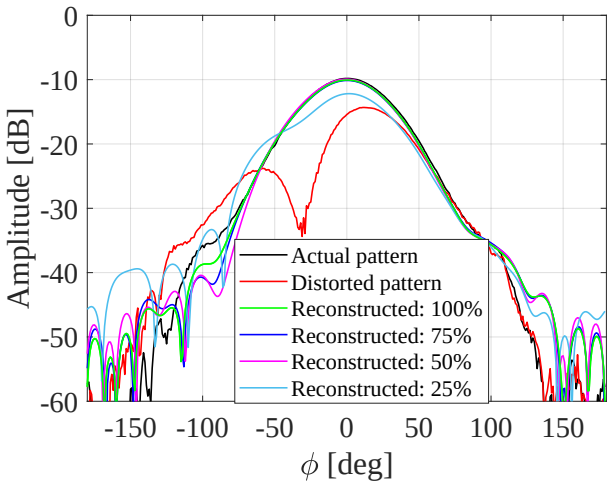

Fig. 19. The reconstructed pattern using different lengths of probe movement.

assumed to be contributed by the echo from $-45°$ and the LOS path. The derived number should be larger than 8.4 positions when the window function is applied. Thus we selected the probe position index with the spacing of 2, 3, and 4, i.e., the index $[1, 3, 5, ...37]$ $(M = 19)$, $[1, 4, 7, ...37]$ $(M = 13)$, and $[1, 5, 9, ...37]$ $(M = 10)$, respectively, to perform the proposed algorithm. The recovered results are shown in Fig. 18, and the excellent matches validated the effectiveness of the proposed criterion, and the peak deviation is only 0.2 dB.

From Fig. 17, it can be found that the reflection path is actually from around $-28°$. The derived required number of probe locations is $M = 5.1$, and at least 6 locations should be moved. As expected, when $M = 5$, obvious pattern distortion can be observed in Fig. 18. Using (27), the obtained minimum length of probe movement for algorithm implementation is $\hat{D} = 0.183m$. Fig. 19 shows the patterns reconstructed with the lengths of $100\%\hat{D}$, $75\%\hat{D}$, $50\%\hat{D}$, and $25\%\hat{D}$. As the movement length decreases, larger deviations are introduced. However, the main lobe and gain can still be well obtained with more than $50\%\hat{D}$. It is because though zero-frequency pollution is introduced, its contribution is not too significant, leading to marginal effects.

VI. Conclusion

In this paper, a novel echo suppression method with a single-frequency phaseless measurement is proposed to recover the antenna gain pattern measured in the non-anechoic chamber. With the proposed method, we first conduct the pattern measurement for a known reference antenna to extract the multipath characteristics (chamber environment). After that, we repeat the measurement for the AUT, and then we recover the free space antenna pattern of the AUT by compensating the multipath characteristics obtained with the reference antenna from the AUT measurement. The proposed strategy using amplitude-only information enables true OTA measurement for antenna pattern, negating the need for complex-signal measurement.

The simulation and measurement results demonstrate the excellent performance of the proposed method for antenna measurement. Compared to the other pattern reconstruction algorithms with non-anechoic measurement, the proposed method reconstructs the true AUT pattern with single-frequency power-only data. Thus, the proposed method can be implemented with the RSP reported by the DUT in active measurement or with the spectrum analyzer in passive measurement. On the other hand, the proposed method can be implemented with a few probe locations and easily automated. Furthermore, the proposed method was demonstrated to be robust compared to the conventional spatial deconvolution algorithm with complex measurement. Comprehensive analyses and systematic guidelines are provided for the proposed echo suppression method. $M = 6$ measurement locations (totally 12 measurements for AUT and reference antenna) are required to reconstruct the accurate AUT pattern in the experiment. It demonstrates that the proposed correction algorithm can reconstruct the antenna pattern based on single-frequency power measurement, however, at a cost of longer measurement time.

To further reduce the required measurement length, one can develop an improved processing method to extract the clean direct components in (12), which will be our future research. In this work, the feasibility of the proposed algorithms for 2-D antenna measurement is demonstrated. In future research, we will exploit the 3-D spatial deconvolution principle to recover the 3-D antenna pattern.

References

[1] B. Fourestie, Z. Altman, and M. Kanda, "Anechoic chamber evaluation using the matrix pencil method," *IEEE Trans. Electromagn. Compat.*, vol. 41, no. 3, pp. 169–174, Aug. 1999.

[2] S. Loredo, G. Leon, S. Zapatero, and F. Las-Heras, "Measurement of low-gain antennas in non-anechoic test sites through wideband channel characterization and echo cancellation [measurements corner]," *IEEE Antennas Propag. Mag.*, vol. 51, no. 1, pp. 128–135, Feb. 2009.

[3] S. Loredo, M. Pino, F. Las-Heras, and T. Sarkar, "Echo identification and cancellation techniques for antenna measurement in non-anechoic test sites," *IEEE Antennas Propag. Mag.*, vol. 46, no. 1, pp. 100–107, Feb. 2004.

[4] Hartmann, J and Fasold, D, "A flexible hardgating system as a diagnostic tool in single and double reflector compact ranges," in *Proc. AMTA*, 1998, pp. 331–336.

[5] Hartmann, J and Fasold, D, "Identification and Suppression of Measurement Errors in Compact Ranges by Application of an Improved Hardgating System," in *Proc. 22nd ESTEC Antenna Workshop*, 1999.

[6] R. S. Adve, T. K. Sarkar, O. M. C. Pereira-Filho, and S. M. Rao, "Extrapolation of time-domain responses from three-dimensional conducting objects utilizing the matrix pencil technique," *IEEE Trans. Antennas Propag.*, vol. 45, no. 1, pp. 147–156, Jan. 1997.

[7] R. A. M. Mauermayer and T. F. Eibert, "Sparse time domain signal representation for echo suppression in antenna measurements," in *Proc. Int. Conf. Electromagn. Adv. Appl. (ICEAA)*, Verona, Italy, Sep. 2017, pp. 1247–1249.

[8] Z. Du, J. I. Moon, S.-S. Oh, J. Koh, and T. K. Sarkar, "Generation of free space radiation patterns from non-anechoic measurements using Chebyshev polynomials," *IEEE Trans. Antennas Propag.*, vol. 58, no. 8, pp. 2785–2790, Aug. 2010.

[9] M. Yuan, J. Koh, T. K. Sarkar, W. Lee, and M. Salazar-Palma, "A comparison of performance of three orthogonal polynomials in extraction of wide-band response using early time and low frequency data," *IEEE Trans. Antennas Propagat.*, vol. 53, no. 2, pp. 785–792, Feb. 2005.

[10] F. J. Cano-Fácila, S. Burgos, F. Martín and M. Sierra-Castañer, "New reflection suppression method in antenna measurement systems based on diagnostic techniques," *IEEE Trans. Antennas and Propag.*, vol. 59, no. 3, pp. 941-949. Mar. 2011.

[11] J. L. Araque Quijano, L. Scialacqua, J. Zackrisson, L. J. Foged, M. Sabbadini, and G. Vecchi, "Suppression of undesired radiated fields based on equivalent currents reconstruction from measured data," *IEEE Antennas Wireless Propag. Lett.*, vol. 10, pp. 314–317, 2011.

[12] L. J. Foged *et al.*, "Echo suppression by spatial-filtering techniques in advanced planar and spherical near-field antenna measurements," *IEEE Antennas Propag. Mag.*, vol. 55, no. 5, pp. 235–242, Oct. 2013.

[13] S. F. Gregson, A. C. Newell, G. E. Hindman, and M. J. Carey, "Advances in cylindrical mathematical absorber reflection suppression," in *Proc. 4th Eur. Conf. Antennas Propag.*, Apr. 2010, pp. 1–5.

[14] D. N. Black and E. B. Joy, "Test zone field compensation," *IEEE Trans. Antennas Propag.*, vol. 43, no. 4, pp. 362–368, Apr. 1995.

[15] J. T. Toivanen, T. A. Laitinen, and P. Vainikainen, "Modified test zone field compensation for small-antenna measurements," *IIEEE Trans. Antennas Propag.*, vol. 58, no. 11, pp. 3471–3479, Nov. 2010.

[16] K. A. Yinusa and T. F. Eibert, "A multi-probe antenna measurement technique with echo suppression capability," *IEEE Trans. Antennas Propag.*, vol. 61, no. 10, pp. 5008–5016, Oct. 2013.

[17] H.-T. Chou and S.-J. Chou, "Multipath suppression for a 2-D far-field pattern in a hybrid antenna measurement facility using single-frequency data," *IEEE Trans. Antennas Propag.*, vol. 64, no. 9, pp. 4083–4087, Sep. 2016.

[18] J. Koh, A. De, T. K. Sarkar, H. Moon, W. Zhao, and M. Salazar-Palma, "Free space radiation pattern reconstruction from non-anechoic measurements using an impulse response of the environment," *IEEE Trans. Antennas Propag.*, vol. 60, no. 2, pp. 821–831, Feb. 2012.

[19] M. Spirlet, C. Geuzaine, and V. Beauvois, "Experimental correction of radiation patterns between electromagnetic environments," *IEEE Trans. Antennas Propag.*, vol. 65, no. 3, pp. 1330–1338, Mar. 2017.

[20] J. Knapp, J. Kornprobst, and T. F. Eibert, "Equivalent source and pattern reconstruction from oversampled measurements in highly-reflective environments," *IET Microw. Antennas Propag.*, vol. 13, no. 13, pp. 2232-2241, Jul. 2019.

[21] J. Knapp and T. F. Eibert, "Near-field antenna pattern measurements in highly reflective environments," *IEEE Trans. Antennas Propag.*, vol. 67, no. 9, pp. 6159–6169, Sep. 2019.

[22] J. van Norel, "Novel APC-methods for accurate pattern determination," M.S. thesis, Tech. Univ. Eindhoven., Eindhoven, Aug. 1993. [Online]. Available: https://pure.tue.nl/ws/portalfiles/portal/46983754/684728-1.pdf.

[23] J. van Norel and V. J. Vokura, "Novel APC-methods for accurate pattern determination," in *Proc. AMTA* , 1993, pp. 385–389.

[24] Y. Zheng and Y. Yu, "Joint estimation of DOA and TDOA of multiple reflections by matrix pencil in mobile communications," *IEEE Access*, vol. 7, pp. 15469–15477, 2019.

[25] TR 38.901, "Study on channel model for frequencies from 0.5 to 100 GHz," 3GPP, Tech. Rep. V14.1.1, July 2017.

[26] A. V. Oppenheim, *Discrete-Time Signal Processing.* Noida, UP, India: Pearson Education India, 1999.